Structural, vibrational, elastic, electronic, and piezoelectric properties of binary γ-GeX and ternary γ-Ge$_2XX'$ monolayers (X, X'= S, Se, and Te)

M. Jahangirzadeh Varjovi,[1,*] Soheil Ershadrad,[2] and Biplab Sanyal[2,†]

[1]*UNAM - National Nanotechnology Research Center and Institute of Materials Science and Nanotechnology, Bilkent University, Ankara 06800, Turkey*

[2]*Department of Physics and Astronomy, Uppsala University, Box-516, 75120 Uppsala, Sweden*

(Received 24 February 2023; accepted 18 April 2023; published 11 May 2023)

The recent synthesis of a new polymorph of two-dimensional (2D) germanium monochalcogenides, namely, γ-GeSe with a four-atomic-layer-thick hexagonal lattice, has received considerable attention due to its novel properties and potential applications. This exciting advancement paves the path for extensive experimental and theoretical investigations on the family of γ-MX crystals in which M and X are elements of group IV and VI, respectively. In this regard, herein we conduct first-principles-based calculations to explore the structural, vibrational, mechanical, electronic, and piezoelectric properties of γ-GeX and Janus γ-Ge$_2XX'$ (X/X' : S, Se, and Te) monolayers. We performed a detailed analysis of the suggested systems' dynamical, thermal, and mechanical stability through phonon-band-dispersion calculations, *ab initio* molecular dynamics (AIMD) simulations, and elastic tensor analyses, respectively, and all six possible nanosheets are found to be stable. The computed Raman spectra of the monolayers reveal that, different from binary systems, the formation of Janus monolayers results in the appearance of additional Raman active modes. The mechanical response of the proposed crystals is examined by calculating in-plane stiffness (Y_{2D}) and the Poisson's ratio (ν) within the elastic regime, and the obtained results ascertain their flexibility. It is found that similar to their binary counterparts, Janus monolayers are indirect-band-gap semiconductors, and their valence-band maxima show a Mexican hat dispersion along the high-symmetry points of the Brillouin zone. Additionally, it is demonstrated that the construction of Janus crystals enhances the piezoelectric coefficients of γ-GeX monolayers, both in the in-plane and out-of-plane directions. Our findings not only provide a comprehensive insight into physical and electronic properties of γ-GeX and γ-Ge$_2XX'$ monolayers but also reveal their promising features for various nanoelectronic and nanoelectrochemical applications.

DOI: 10.1103/PhysRevB.107.195421

I. INTRODUCTION

Two-dimensional (2D) materials, the study of which was boosted after the successful isolation of single-layer (SL) graphene [1], have attracted intense research interest due to their remarkable physical properties and potential applications in advanced devices [2–4]. The quantum confinement enables 2D materials to offer alternative features and new functionalities, unprecedented in their bulk counterparts, promising for applications in current and prospective nanodevices [5]. Recently, phosphorene, a monolayer or multiple layers of black phosphorus (BP), has attracted tremendous attention due to its remarkable properties, such as an inherent direct band gap in monolayer form and high carrier mobility, which make it a useful material in various applications [6,7]. The puckered crystalline form of phosphorene has been synthesized through various techniques, including plasma thinning after mechanical cleavage [8] and liquid exfoliation [9]. Consecutive to its synthesis, isostructural and isoelectronic counterparts of phosphorene such as GeS, GeSe, and GeTe have been a focus of application for thermoelectric devices [10–12]. Lately, GeS nanosheets have been synthesized using vapor deposition or the one-pot strategy, offering the possibility of exfoliating bulk GeS into the monolayer form [13,14]. The symmetry of the fabricated crystal is referred to as α phase, which is the conventional crystalline form of group-IV monochalcogenides [15,16]. Following this progress, various synthesizing techniques were also demonstrated for 2D α-GeX crystals [17,18]. In addition to experimental studies, theoretical calculations have predicted significant electron mobility of α-GeS ($\sim$ 3680 cm^2 V^{-1} s^{-1}), which is larger than that of MoS_2 monolayer [19]. Moreover, the GeSe monolayer, a member of the α-GeX family, has drawn significant interest due to its low thermal conductivity and strong visible-light absorption [20,21]. Zhang *et al.* reported that in the α-GeTe monolayer, the value of figure of merit can reach to 4.23 at 900 K, which is much larger than its bulk counterpart [22]. It is known that the physical properties of 2D

*mirali@bilkent.edu.tr
†Biplab.Sanyal@physics.uu.se

materials with the same chemical formula but different atomic arrangements (polymorphs) can vary significantly from each other [23–25]. Recently, a new configuration of 2D group-IV monochalcogenides, namely, γ-*MX* with an unusual band inversion (Mexican-hat dispersion), has been theoretically proposed by using the density-functional theory (DFT) calculations [26]. Following that, a member of the *MX* family, γ-GeSe, has been successfully synthesized by chemical vapor deposition on the h-BN substrate [27]. In addition to γ-GeSe, very recently, a Si-based member of γ-*MX* (γ-SiTe) has been successfully fabricated and shown to be a semiconductor [28]. Moreover, theoretical investigations have reported that in γ-Ge*X* (*X* : S, Se, and Te) monolayers, the energy band gaps and valley positions, as well as optical absorption peaks, can be modified with strain engineering [29].

In line with ongoing efforts on exploring new 2D materials, the formation of ternary (Janus) configurations from binary crystals has been proposed following the recent synthesis of Janus MoSSe [30,31]. In these materials, the symmetry of structures is lowered by substituting all atoms at one layer of their binary counterpart with a different atom in the same group [32,33]. As two surfaces of these crystals possess different properties, Janus monolayers can exhibit superior physical properties concerning the prior structure [34,35]. It has been shown that in the MoSSe monolayer, broken structural symmetry can lead to distinct features such as large Rashba spin splitting and nonzero out-of-plane piezoelectricity [35,36]. In other studies it was reported that upon the formation of Janus monolayers, additional peaks appear in the Raman spectrum [37,38]. To date, the investigations of the *MX* family are mainly concentrated on conventional phases of germanium monochalcogenides, and a comprehensive study focusing on newly realized γ-Ge*X* crystals and their Janus counterparts has not been performed. With this motivation, in the present study we systematically studied the structural, vibrational, mechanical, electronic, and piezoelectric properties of binary γ-Ge*X* and ternary γ-Ge_2XX' (*X*/*X*′ : S, Se, and Te) monolayers. In the first part, the ground-state configurations of the γ-Ge*X* and γ-Ge_2XX' monolayers are obtained, and the relevant structural parameters and cohesive energies are reported. Next, the stability of the proposed systems is tested from the dynamical and thermal aspects based on phonon dispersion and *ab initio* molecular dynamics (AIMD) simulations, respectively. The vibrational properties are investigated, and the corresponding Raman spectra and atomic displacements of the optical phonon modes are presented. Then the mechanical response in the elastic regime and the electronic properties are examined. Finally, the piezoelectric response is studied, and computed piezoelectric coefficients are obtained.

II. METHODOLOGY

In this study, all first-principles calculations were performed within the framework of density functional theory (DFT) [39,40] using the Vienna *Ab initio* Simulation Package (VASP) [41–44]. The projector augmented wave [45] method was employed to describe the electron-ion interaction. The exchange-correlation potential was treated by the generalized gradient approximation (GGA) with the Perdew, Burke, and Ernzerhof (PBE) [46] functional. For the calculation of electronic band structures, spin-orbit coupling (SOC) was also taken into account [47]. In addition, the hybrid functional of Heyd-Scuseria-Ernzerhof (HSE06) was employed with SOC to obtain more accurate energy band gaps [48,49]. The HSE06 functional was developed by combining 25% of nonlocal Fock exchange with 75% of PBE exchange and 100% of PBE correlation energy and screening length of $\lambda = 0.2$ Å^{-1}. The value of the kinetic-energy cut-off for the plane-wave basis set in all calculations was taken as $\hbar^2 \mid \mathbf{k} + \mathbf{G} \mid^2/2m = 520$ eV, and the total energy was minimized until its variation in the sequential steps became 10^{-5} eV. During structural optimization (ionic positions and lattice constants), the maximum allowed Hellmann-Feynman forces were reduced to 0.01 eV/Å, and the maximum pressure on the unit cell was less than 1 kbar. To hinder any spurious (unphysical) interaction in the nonperiodic direction, a vacuum layer of ∼15 Å was used. For structural relaxation, the Brillouin zone (BZ) integration was carried out on a Γ-centered $16 \times 16 \times 1$ uniform *k*-point mesh obtained within the Monkhorst-Pack scheme [50]. The phonon band dispersions were calculated for $4 \times 4 \times 1$ supercells within GGA using the small-displacement method as implemented in the PHONOPY code [51]. To investigate the thermal stability, AIMD simulations were performed by using a microcanonical ensemble at constant temperatures (300 and 600 K) with a total simulation time of 10 ps and 1 fs time step. The vibrational frequencies and their corresponding off-resonant zone-centered Raman activities were calculated using the finite displacement approach. For this purpose, initially, each atom in the primitive cell was distorted by 0.01 Å, and the correlated dynamical matrix was computed. Following that, the vibrational modes were determined by directly diagonalizing the dynamical matrix. The Raman activity of each phonon mode was estimated by deriving the macroscopic dielectric tensor at the Γ point using the small difference approach. The Raman spectra were generated using a suitable Gaussian broadening acquired from the results of Raman calculations [34]. Additionally, both elastic constants and piezoelectric coefficient tensors were calculated using density functional perturbation theory (DFPT) with a sufficiently large *k*-point sampling and cutoff energy of 700 eV. To analyze the net charge on atoms and understand the bond characteristics of the examined monolayers, the Bader technique was employed [52].

III. RESULTS AND DISCUSSION

A. Atomic structure and energetics

In accordance with the geometry of synthesized 2D crystals of γ-GeSe and γ-SiTe, we first started with the structural optimization of binary γ-Ge*X* (*X* = S, Se, and Te) monolayers. The crystals possess a hexagonal lattice with the symmetry of D_{3d} and space group of $P\bar{3}m1$ (No. 164). The schematic representation of the γ-Ge*X* monolayers is demonstrated in Figs. 1(a) and 1(b). The primitive cell of the nanosheets contains four sublayers (*X* − Ge − Ge−*X*) which are held together with strong covalent bonding. The single layers (SLs) of γ-Ge*X* hold an inversion symmetry in which the symmetry plane lies on the horizontal plane between two Ge atoms. As given in Table I, for the γ-GeS, γ-GeSe, and γ-GeTe

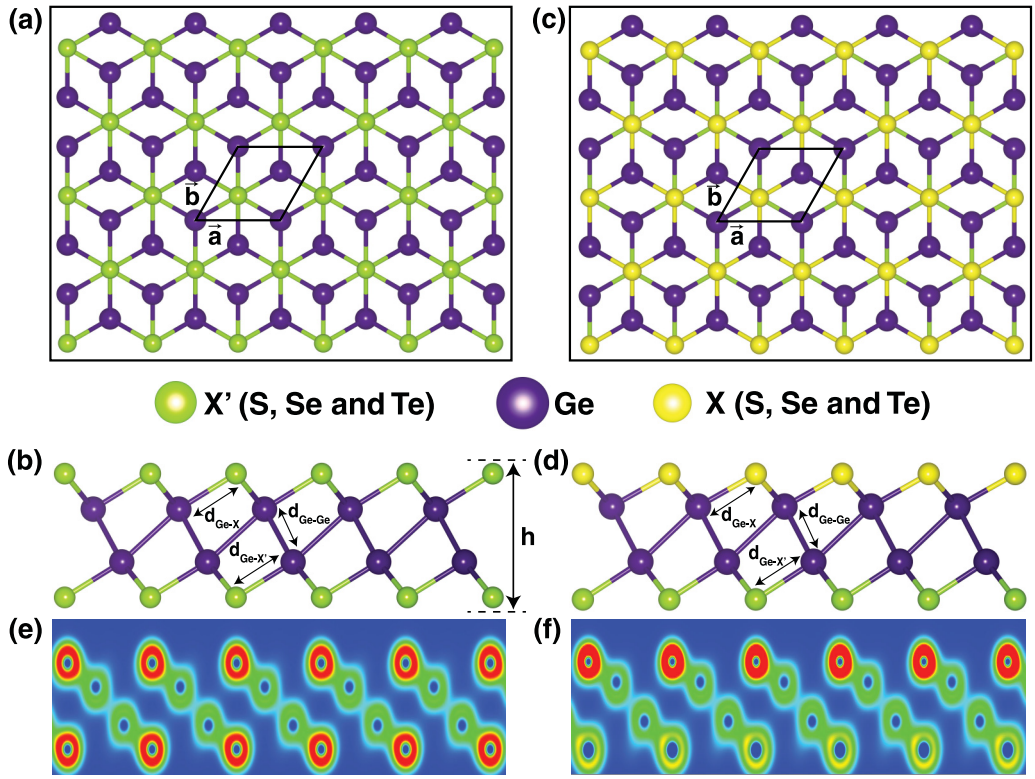

FIG. 1. For γ-GeX and γ-Ge$_2XX'$ monolayers, (a, c) top, (b, d) side views of the crystal structures, respectively, and (e, f) the corresponding total charge distribution profile of the binary and ternary systems, respectively. The charge profile is represented by a color scheme with linear scaling from blue (lowest) to red (highest). The relevant geometrical parameters are labeled.

nanosheets, the optimized lattice constants (**a**=**b**) are calculated to be 3.65, 3.81, and 4.06 Å, respectively, which are in good agreement with the reported values of previous studies [29]. The computed structural properties of binary γ-GeX monolayers, such as in-plane lattice constants, bond length between the atoms, and the thickness (**h**) of the structures (which is defined as normal distance between the boundary chalcogen atoms), enlarges with the atomic radius of chalcogen atoms. Once the binary γ-GeX systems are obtained, ternary γ-Ge$_2XX'$ monolayers are constructed by replacing one of the X layers with a different chalcogen (X') atom. In the present study, the ingredient of the top atomic layer is the light chalcogen atom (X), while the heavier chalcogen element (X') makes up the bottom layer. Top and side views of the crystal structure of the γ-Ge$_2XX'$ monolayers are illustrated in Figs. 1(c) and 1(d), respectively. In the Janus structures, the two Ge atoms are sandwiched between upper chalcogenide X and bottom chalcogen X' atoms. Taking into account the broken inversion symmetry in z direction, the lattice constants (**a**, **b**) are independently relaxed but found to be equal. This indicates that the hexagonal lattice is also conserved in ternary systems; however, their symmetry is changed to C_{3v} and space group of $P3m1$ (No. 156). The structural properties of the Janus γ-Ge$_2XX'$ crystals are also summarized in Table I. The calculated lattice parameters (**a**=**b**) of ternary germanium monochalcogenides are 3.73, 3.87, and 3.94 Å for γ-Ge$_2$SSe, γ-Ge$_2$STe, and γ-Ge$_2$SeTe, respectively. Similar to the binary crystals, **a** increases while going down the chalcogen group. It is found that the lattice constants of Ge$_2XX'$ nanosheets are larger (smaller) than those of GeX(GeX') structures. As a

TABLE I. For monolayers of γ-GeX and γ-Ge$_2$XX$'$, we present the optimized lattice constants, **a** and **b**; atomic bond lengths, $d_{\mathrm{Ge}-X}$, $d_{\mathrm{Ge}-X'}$, and $d_{\mathrm{Ge}-\mathrm{Ge}}$; thickness, h; average charge transfer from Ge to X, $\Delta\rho_{(\mathrm{Ge}-X)}$ and Ge to X$'$, $\Delta\rho_{(\mathrm{Ge}-X')}$; calculated work functions for two different surfaces and their differences, Φ_X, $\Phi_{X'}$, and $\Delta\Phi$, and the cohesive energy per atom, E_C.

Crystal structure	a (Å)	b (Å)	$d_{\mathrm{Ge}-X}$ (Å)	$d_{\mathrm{Ge}-X'}$ (Å)	$d_{\mathrm{Ge}-\mathrm{Ge}}$ (Å)	h (Å)	$\Delta\rho_{(\mathrm{Ge}-X)}$ (e$^-$)	$\Delta\rho_{(\mathrm{Ge}-X')}$ (e$^-$)	Φ_X (eV)	$\Phi_{X'}$ (eV)	$\Delta\Phi$ (eV)	E_C (eV/atom)
γ-GeS	3.65	3.65	2.45	2.45	2.96	4.57	0.69	0.69	4.81	4.81	0.00	3.68
γ-GeSe	3.81	3.81	2.58	2.58	2.98	4.73	0.53	0.53	4.55	4.55	0.00	3.42
γ-GeTe	4.06	4.06	2.78	2.78	3.02	4.90	0.30	0.30	4.26	4.26	0.00	3.14
γ-Ge$_2$SSe	3.73	3.73	2.47	2.56	2.97	4.63	0.69	0.52	5.02	4.54	0.48	3.55
γ-Ge$_2$STe	3.87	3.87	2.50	2.73	3.01	4.73	0.69	0.28	5.42	4.40	1.02	3.37
γ-Ge$_2$SeTe	3.94	3.94	2.61	2.75	3.01	4.81	0.53	0.29	4.89	4.31	0.58	3.27

result, the upper and lower layers of these structures experience different types of induced biaxial strains (i.e., the X side undergoes a tensile strain, whereas the X' side is under compressive strain). In the Ge_2SSe structure, the atomic bond lengths between Ge − S and Ge − Se pairs are 2.47 and 2.56 Å, respectively. For the Ge_2STe monolayer, the Ge − S bond length is 2.50 Å, whereas that of Ge − Te is 2.73 Å. In SL-Ge_2SeTe, the atomic bond lengths Ge − Se and Ge − Te are calculated as 2.61 and 2.75 Å, respectively. As expected, the bond length between two germanium atoms (Ge − Ge) in the structures remains almost the same. In addition, the obtained values of **h** for γ-Ge_2SSe, γ-Ge_2STe, and γ-Ge_2SeTe structures are 4.63, 4.73, and 4.81 Å, respectively. Not surprisingly, for fixed X, the **h** of the crystals thickens with increasing atomic radius of X' atoms. According to Bader charge analyses, the charge donation from Ge atoms to neighboring chalcogens in binary crystals is symmetric and estimated to be 0.69, 0.53, and 0.30 e^- for γ-GeS, γ-GeSe, and γ-GeTe monolayers, respectively. Charge transfer ($\Delta\rho$) in structures decreases while going down the chalcogen group associated with the fact that $\Delta\rho$ depends on the electronegativity difference between Ge and X atoms. The same trend of $\Delta\rho$ between Ge and X can also be found in the Janus monolayers; however, the amount of transferred charge is different. All obtained results of Bader analyses for both binary γ-GeX and ternary γ-Ge_2XX' are summarized in Table I. The corresponding data from charge analysis in Ge_2SSe demonstrate that the charge depletion from the upper (lower) Ge to S (Se) is 0.69 (0.52) e^-. In the SL-Ge_2STe monolayer, 0.69 and 0.28 e^- are donated from adjacent Ge atoms to S and Te, respectively, which results in a strong polarization in the z direction. Moreover, 0.53 and 0.29 e^- charges are donated to Se and Te atoms from neighboring Ge atoms, respectively. The covalent character of the bonds between constituent atoms in binary and ternary systems is also shown in Figs. 1(e) and 1(f), respectively. The planar average of the electrostatic potential of the examined systems is computed, and their variation along the z axis is displayed in Fig. S1, Supplemental Material [53]. The work function (Φ) can be calculated as $\Phi = E_{Vac.} - E_{Fermi}$, where $E_{Vac.}$ is the energy level of a stationary electron in the vacuum and E_{Fermi} is the Fermi energy of the corresponding crystal. Since the bottom and top layers of binary γ-GeX structures are formed by identical atoms, no potential difference can be found between the two layers. Therefore both sides have the same value of thermionic work function ($\Phi_X = \Phi_{X'}$). The acquired values of Φ_X for γ-GeS, γ-GeSe, and γ-GeTe are 4.81, 4.55, and 4.26 eV, respectively, which are within the same range as the reported value for α-GeS monolayer (4.65) [54]. On the other hand, the charge difference between the surfaces, which originates from the different types of atoms on boundary layers, affects the magnitude of the work function on each side ($\Phi_X \neq \Phi_{X'}$), as listed in Table I. It is noticed, in the Janus structures, that the work function difference between two layers ($\Delta\Phi$) is proportional to the magnitude of charge difference between two sides. The cohesive energy per atom (E_C) of the examined structures can be computed using the following relation:

$$E_C = \frac{[2E_T(\mathrm{Ge}) + E_T(X) + E_T(X')] - [E_T(\mathrm{Ge_2}XX')]}{4}, \quad (1)$$

where E_T(Ge), $E_T(X)$, and $E_T(X')$ are the single atom energies of Ge, X, and X' elements, respectively, $E_T(Ge_2XX')$ corresponds to the total energy of the crystal structures, and the denominator is the total number of atoms (4) in the primitive cell. It is worth noting that X and X' are the same in binary monolayers. As presented in Table I, E_C gradually decreases as **a** enlarges, correlating with bond weakening in the systems, which is attributable to the reduction in charge transfer between Ge and chalcogen atoms. The cohesive energies of the examined monolayers are in the range of 3.14–3.68 eV/atom, which is comparable with those of δ-GeS (3.61 eV/atom) and δ-GeSe (3.37 eV/atom) [55]. Moreover, Table S1 (see Supplemental Material [53]) includes a number of reported cohesive energies for the α and β phases for comparison.

B. Dynamical stability

After unveiling the structural features, the dynamical stability of the suggested systems is analyzed by calculating their phonon dispersion relations, and the corresponding phonon band structures are illustrated in Fig. 2. In the analysis of phonon spectra, whenever an imaginary frequency is present, the structure is dynamically unstable since there is no restoring force against the displacement of atoms along the particular eigenmode. In the considered systems, all phonon modes possess positive frequency, indicating stability at low temperatures. The transverse acoustic (TA) and the longitudinal acoustic (LA) branches show linear dispersions near the Γ point, whereas the out-of-plane flexural acoustic (ZA) branch displays a quadratic relation, as the force constants associated with the transverse vibrations decay rapidly in this mode [56]. It can be observed from Fig. 2 that with increasing the atomic weight of the chalcogen atom, the frequencies of phonon modes (including the maximum vibrational frequency, ω_{max}) in the entire frequency range gradually shrink in both binary and ternary crystals. A detailed analysis of the force constant matrices ascertains that the origin of vibrational frequency narrowing is not only due to the increased mass of the X or X' atoms but is also associated with the reduction of bond strength among the atoms. Generally, the narrower band dispersion of phonons in 2D systems leads to the suppression of their group velocity. Additionally, in both γ-GeX and γ-Ge_2XX' structures, there are frequency ranges where the acoustic and optical phonon modes overlap with each other, which results in robust acoustic and optical scattering and consequently, low thermal conductivity. To interpret the phonon spectra, we also performed phonon density of states (PhDOS) calculations, and the results are presented in Fig. S2, Supplemental Material [53]. The PhDOS diagrams indicate that the high-frequency phonon modes are attributed to the vibrational of lighter elements in the systems, whereas the movement of heavy atoms predominates the lower-frequency phonon modes. As an example, in γ-Ge_2STe monolayer, low-frequency phonon modes are mainly characterized by the vibrations of Te, midrange frequency is attributed largely to Ge, and S atoms dominate high-frequency vibrations. In phonon spectra of the examined systems, a gap is noticed between lower- and higher-frequency optical phonon modes, which is due to the mass difference and the binding strength between the constituent atoms in the nanosheets.

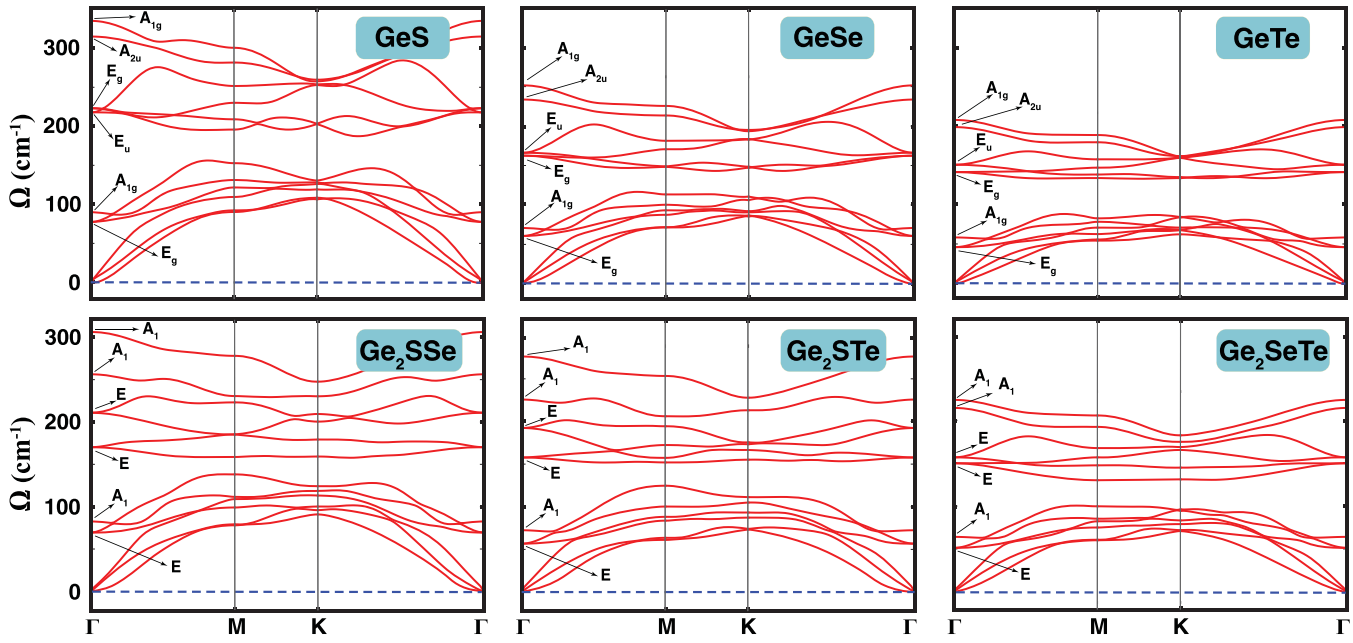

FIG. 2. Phonon dispersion spectra of γ-GeX and γ-Ge$_2XX'$ monolayers.

Associated with analyzing the phonon-band dispersions, we studied the thermal properties of suggested crystals, since understanding a material's thermal behavior is essential for applications in nanoscale devices at finite temperatures. Accordingly, thermal properties of the γ-GeX and γ-Ge$_2XX'$ monolayers are investigated in terms of isovolume heat capacity (C_V) as a function of temperature. C_V refers to a material's ability to store heat for a given temperature range. Figure 3 presents C_V of γ-GeX and γ-Ge$_2XX'$ structures up to 600 K, at which structural stability is still preserved. Our results indicate that similar to bulk materials, all C_V curves increase rapidly in the low-temperature regime and approach the classical Dulong-Petit limit of $3R$, where R denotes the universal gas constant. It can be noted that either at low or room temperatures, C_V moderately increases down the chalcogen group (i.e., C_V follows a sequence of γ-GeS $<$ γ-Ge$_2$SSe $<$ γ-Ge$_2$STe $<$ γ-GeSe $<$ γ-Ge$_2$SeTe $<$ γ-GeTe), which is correlated with the shift of the optical vibrational modes with chalcogen atoms [57]. In addition, as a general feature of 2D materials, the rise of C_V at low temperatures is not linear; rather, the relation is more likely quadratic and scales with $T^{2/n}$ ($n > 0$). Accordingly, for the studied systems, n is estimated between the values of 1.02 and 1.30, with 1.02 for GeS and 1.30 for GeTe, respectively. As the frequency of acoustic phonon modes (ω) near the Γ point scales with the momentum (q) by $\omega = q^n$ [58,59], the dispersion of phonon frequency is found to be $\omega = q^{1.02-1.30}$. As mentioned, LA and TA phonon modes change linearly with q ($\omega = q$), whereas ZA vibrational mode shows a parabolic dispersion($\omega = q^2$). This means that in γ-GeX and γ-Ge$_2XX'$ monolayers, the main contribution to the C_V arises from in-plane LA-TA modes.

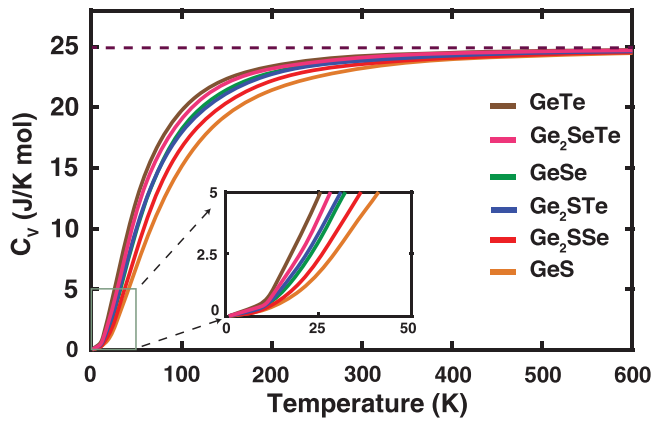

FIG. 3. The variation of isovolume heat capacity (C_V) for γ-GeX and γ-Ge$_2XX'$ monolayers with temperature. The low-temperature limit is displayed as inset.

To further check the stability of the structures at elevated temperatures, we performed AIMD simulations at 300 and 600 K for 10 ps. A $4 \times 4 \times 1$ supercell was generated for the examined nanosheets to remove the unit-cell size limitations. Plotting the total energy variation allows us to track the alternation of crystalline morphology, as the total energy of the monolayers is sensitive to any bond breaking and bond formation. The variation of energy with respect to the simulation time and the final snapshots of the resulting geometries taken at 300 K and 600 K are shown in Fig. 4 and Fig. S3, Supplemental Material [53], respectively. Based on the results of AIMD simulations, gradient values of total energies fluctuate around a constant value. From the structural point of view, aside from slight distortions, which are not sufficient enough to break the bonds between the constituent elements, the crystalline forms of the γ-GeX and γ-Ge$_2XX'$ are preserved even at elevated temperatures and confirm the thermal stability. The thermal stability of the studied crystals is critical for thermoelectric device applications, which often operate at high temperatures.

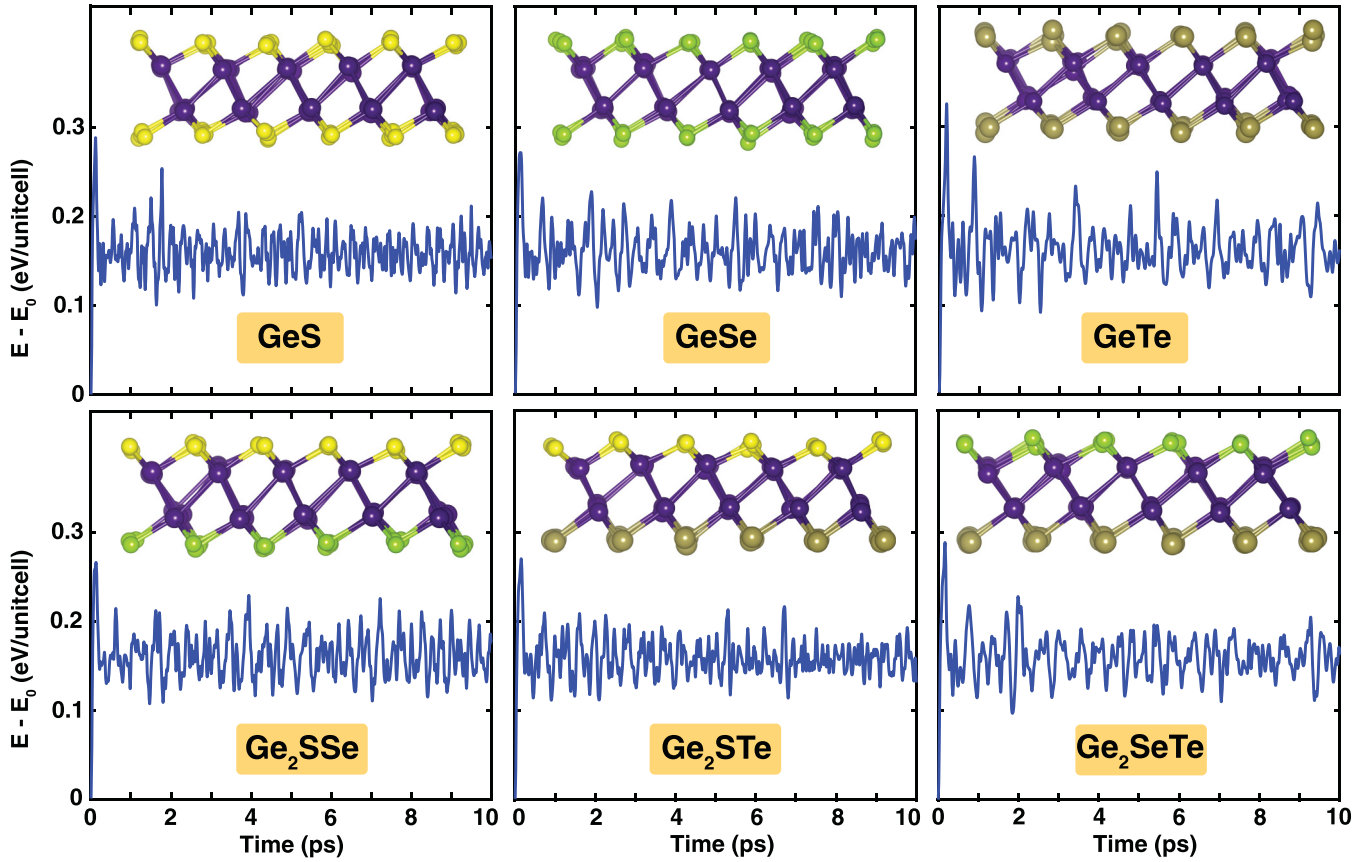

FIG. 4. The variation of total energy with respect to time at 300 K, with the snapshot of atomic configuration for each structure at the end of the simulation illustrated as inset.

C. Vibrational properties

As vibrational properties and the corresponding Raman spectra of the materials are closely related to their geometrical structure, their analysis can be a useful tool for getting insight into the physical features associated with lattice symmetries. As mentioned above, the binary γ-GeX monolayers possess D_{3d} symmetry and a space group of $P\bar{3}m1$ (No. 164). Accordingly, the nine optical phonon modes at the Γ point are either nondegenerate or doubly degenerate. The group theory analysis of binary systems reveals that the irreducible representation for the optical phonon modes at the Γ point can be expressed by $\Gamma^{D_{3d}} = 2E_g + E_u + 2A_{1g} + 1A_{2u}$, where E_g and E_u phonon modes are attributed to the doubly degenerate in-plane vibrations, whereas A_{1g} and A_{2u} modes represent vibrations along the out-of-plane direction. Among the vibrational modes, the E_g and A_{1g} are Raman active (RA) since they correspond to quadratic functions in the character table of D_{3d} symmetry, while E_u and A_{2u} are infrared active (IRA) modes as these modes correspond to the linear functions. Therefore the vibrational mode analysis of γ-GeX monolayers should reveal four peaks corresponding to the RA and two peaks for IRA modes, respectively. In a Raman experiment, a beam of light is focused onto the sample, and the scattered photons are immediately collected. A dispersion of the intensity of the shifted light with respect to the frequency shift results in a Raman spectrum of the material. According to Raman theory, Raman active vibrational modes are associated with inelastically dispersed photons originating from the oscillation of dipole moments of the crystal. The calculated Raman spectra of binary γ-GeX crystals are illustrated in Fig. 5(a). To identify the origin of the Raman peaks, the atomic displacements of the RA modes are annotated on each spectrum. By going down the X atoms in the structures, the Raman spectra shift toward lower frequencies, mainly due to the increased mass and weakening of the bond strength of Ge and the X atoms. For the γ-GeSe monolayer, the theoretical Raman spectra can be compared with the results of experimental data. Lee *et al.* demonstrated that the first and second A_{1g} Raman peaks appear at frequencies of 90 and 257 cm^{-1}, respectively, while in our results they appear at 71 and 251 cm^{-1}, respectively. In addition, the first and second E_g Raman peaks in the experiment are observed at 67 and 164 cm^{-1}, respectively. On the other hand, calculated RA mode for $E_g(1)$ and $E_g(2)$ appear at 61 and 166 cm^{-1}, respectively. The comparisons reveal that our computed results are in good agreement with the experimental findings on synthesized γ-GeSe [27]. The common vibrational motion of optical phonon modes of the binary γ-GeX structures is illustrated in Fig. 5(b). As shown in the figure, the first optical phonon mode with the lowest energy is the same for all structures and belongs to E_g representation. The first E_g phonon mode [i.e., $E_g(1)$] arises from the in-plane symmetric vibration of GeX pairs. The low-energy E_g mode is followed by the A_{1g} mode, which represents the out-of-plane vibration of GeX pairs against each other while the vibration of heavier atoms is more dominant. The $E_g(2)$ mode corresponds to the dominant opposite in-plane vibration of lighter elements in the

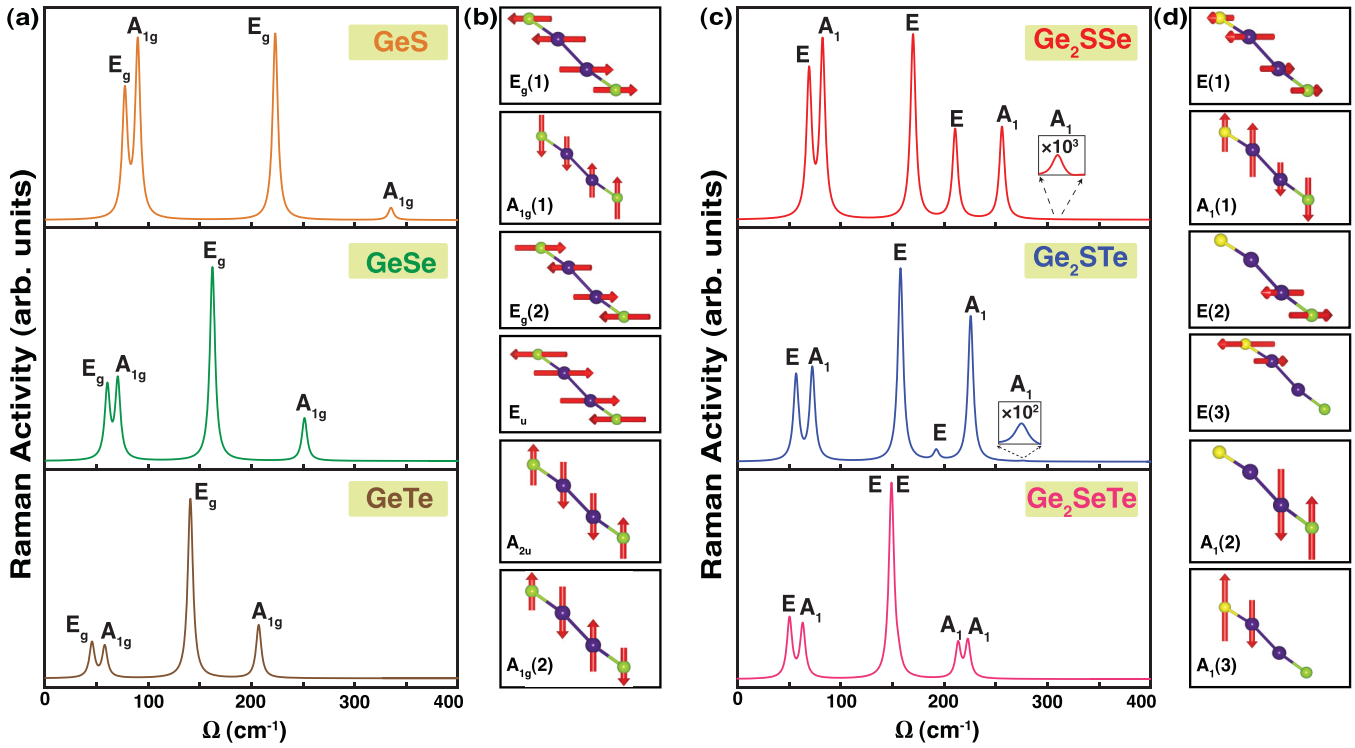

FIG. 5. Calculated first-order Raman spectra [(a), (c)] and the corresponding atomic displacement of zone-centered vibrations [(b), (d)] of binary γ-GeX and ternary γ-Ge$_2XX'$ structures, respectively.

structures. The E_u and A_{2u} phonon modes correspond to the asymmetric in-plane and out-of-plane vibrations of GeX pairs against each other, respectively. The $A_{1g}(2)$ mode is attributed to the vibrations of GeX sublayers in the opposite out-of-plane direction, while the lighter elements in the systems contribute the most to the vibration. Differing from the γ-GeX monolayers, Janus γ-Ge$_2XX'$ crystals exhibit additional Raman active modes due to the broken inversion symmetry along the z direction by replacing X layers with another chalcogenide atom. According to our group theory analysis, the irreducible representation of the optical phonon modes of the ternary systems can be described by $\Gamma^{C_{3v}} = 3A_1 + 3E$, where the E modes correspond to the doubly degenerate in-plane displacements, whereas the nondegenerate A_1 modes are assigned to the vibration of the atoms along the out-of-plane direction. Both A_1 and E vibrational modes are Raman active modes, as they correspond to quadratic functions in the character table of C_{3v} symmetry. Therefore, theoretical Raman spectra of the Janus γ-Ge$_2XX'$ structures should exhibit six typical Raman peaks. The calculated Raman activity of the ternary monolayers is depicted in Fig. 5(c), and the corresponding atomic displacements of each peak in the Raman spectra are labeled. Similar to binary structures, increasing the lattice parameters of Janus monolayers results in a redshift of Raman spectra. Our results indicate that the most intense Raman peak belongs to the second E vibrational mode. The intensity of Raman peaks is correlated with the contribution of macroscopic dielectric constants of vibrational modes to the Raman tensors. As two chalcogenide atoms are different in Janus crystals, their vibrations are not symmetric with respect to the plane that lies horizontally between two Ge atoms. Figure 5(d) presents the atomic displacement of each Raman peak in the γ-Ge$_2XX'$ monolayers. The first optical phonon mode with the lowest frequency belongs to E representation. In this mode, the GeX pair vibrates in the opposite in-plane direction of the GeX' pair. The first E mode is followed by the A_1 mode, and in this mode, the GeX and GeX' pairs move in opposite out-of-plane direction. The character of the second E mode reveals that the Ge and X' atomic planes move in the opposite in-plane direction, while the vibration of the GeX pair is weak and can be ignored. On the other hand, the third E mode corresponds to the dominant opposite in-plane vibration of Ge and X atoms. The vibrational motion of the second A_1 mode arises from the out-of-plane vibrations of the Ge and X' pair along the z axis, whereas the third A_1 mode is mainly originated from the vibration of Ge and X in the out-of-plane direction. Our results on the Raman spectra of γ-GeX and γ-Ge$_2XX'$ monolayers can be used as guidelines for an effective characterization of synthesized compounds.

D. Mechanical properties

After revealing the dynamical and thermal stability of binary γ-GeX and ternary γ-Ge$_2XX'$ structures, the elastic strain tensors (C_{ij}) are calculated to evaluate their elastic stability and explore the mechanical properties of the crystals using the stress theorem [60,61]. As listed in Table II, the values of C_{ij} are found to be positive for studied nanosheets, and these values satisfy the Born and Huang criteria [62,63] [$C_{11} > |\, C_{12}\,|$ and $C_{66} = (C_{11} - C_{12})/2 > 0$] for a 2D hexagonal lattice, verifying the elastic stability. The mechanical response of the homogeneous 2D materials within the elastic regime can be investigated in terms of in-plane stiffness (Y_{2D}) and Poisson's ratio (ν). For a discussion on a material's

TABLE II. For monolayers of γ-GeX and γ-Ge_2XX', energy band gaps at the level of GGA-PBE, E_g^{PBE}; GGA-PBE + SOC, $E_g^{PBE-SOC}$; HSE06 + SOC, $E_g^{HSE-SOC}$; the locations of VBM and CBM edges in the BZ; relaxed-ion elastic coefficients C_{ij}, in-plane stiffness Y_{2D}, and Poisson's ratio ν, piezoelectric stress coefficients e_{ij}, and the corresponding piezoelectric strain coefficients d_{ij}.

Structure	E_g^{PBE} (eV)	$E_g^{PBE-SOC}$ (eV)	$E_g^{HSE-SOC}$ (eV)	VBM/CBM (−)	C_{11}=C_{22} (N/m)	C_{12} (N/m)	Y_{2D} (N/m)	ν (−)	e_{11} (pC/m)	e_{31} (pC/m)	d_{11} (pm/V)	d_{31} (pm/V)
γ-GeS	0.72	0.72	1.12	K-Γ/Γ	81.56	26.03	73.25	0.32	0.60	0.02	1.08×10^{-2}	0.18×10^{-3}
γ-GeSe	0.54	0.53	0.94	K-Γ/Γ	76.56	20.25	71.20	0.26	0.58	0.14	1.03×10^{-2}	1.44×10^{-3}
γ-GeTe	0.54	0.52	0.87	K-Γ/Γ	69.44	13.49	66.81	0.19	0.44	0.32	0.78×10^{-2}	3.85×10^{-3}
γ-Ge_2SSe	0.73	0.70	1.11	K-Γ/Γ	78.91	23.36	72.00	0.30	320	16	5.76	0.15
γ-Ge_2STe	0.85	0.79	1.16	K-Γ/M	72.55	21.01	66.46	0.29	683	30	13.25	0.32
γ-Ge_2SeTe	0.75	0.72	1.07	K-Γ/M	71.91	17.31	67.74	0.24	396	17	7.25	0.19

resistance to distortion under mechanical load, these two terms are crucial to be determined. Y_{2D} is defined as a measure of the rigidity or flexibility of a material and depends on both the crystalline structure and the bonding nature between constituent atoms. Based on the obtained values of C_{ij}, Y_{2D} of the 2D hexagonal systems are calculated using the expression $Y_{2D} = (C_{11}^2 - C_{12}^2)/C_{11}$, and the results are summarized in Table II. The computed Y_{2D} are isotropic and vary in the range of 66.46–73.25 N/m, which is smaller than the reported values of binary MoX_2 and Janus $MoXX'$ monolayers, indicating the elastic character of GeX and Ge_2XX' crystals [64]. In addition, the variation of Y_{2D} as a function of **a** is shown in Fig. 6(a). An overall decline in the values of Y_{2D} is observed as **a** increases. It can be attributed to the weakening of the bond between the atoms as E_C also follows a similar pattern. The decreasing trend reveals that as the Y_{2D} decreases, the corresponding restoring forces in the monolayers become more effective in a shorter range of applied force. Next, we analyzed the Poisson's ratio (ν) of the suggested systems. ν is an intrinsic mechanical property of a material and can be described as the negative transverse contraction strain divided by longitudinal extension strain. Based on C_{ij}, ν is determined by using the relation $\nu = C_{12}/C_{11}$, and the computed results are listed in Table II. The values of ν for γ-GeS, γ-GeSe, and γ-GeTe monolayers are 0.32, 0.26, and 0.19, respectively, which agree with the literature [29]. For Janus crystals, ν displays small changes from γ-Ge_2SSe to γ-Ge_2SeTe (0.30 for γ-Ge_2SSe, 0.29 for γ-Ge_2STe, and 0.24 for γ-Ge_2SeTe), and when compared to their binary counterparts, ν of γ-Ge_2XX' lies between γ-GeX and γ-GeX'. Similar to Y_{2D}, ν also decreases by increasing **a** (elongation of bond length), as it is shown in Fig. 6(b). In addition, according to the Christensen criterion, the threshold for the ductile/brittle transition in the materials is $\nu \approx 2/7$ [65]. Therefore the monolayers with larger $\nu > 2/7$ can be considered ductile, and those with a lower value of 2/7 possess a brittle character. Accordingly, γ-GeSe, γ-GeTe, and Janus γ-Ge_2SeTe nanosheets possess a brittle nature.

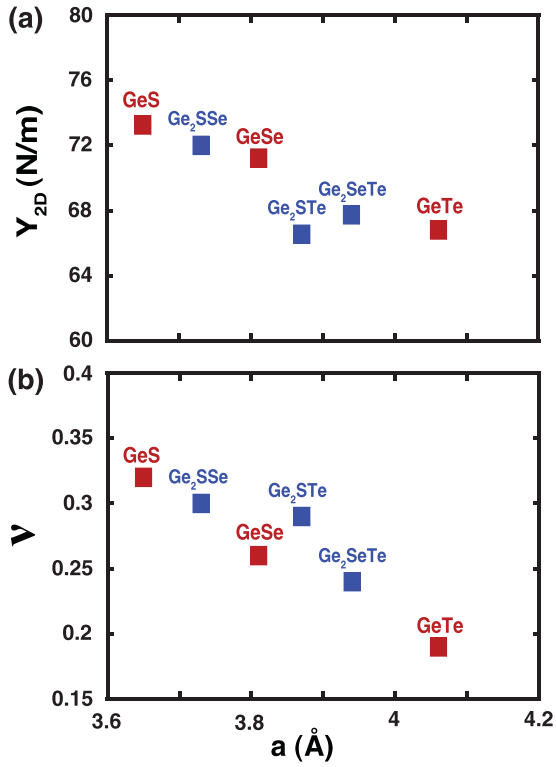

FIG. 6. (a) The variation of in-plane stiffness (Y_{2D}) and (b) Poisson's ratio (ν) as a function of lattice constant for γ-GeX and γ-Ge_2XX' monolayers.

E. Electronic properties

Next, the electronic properties of the γ-GeX and γ-Ge_2XX' monolayers are investigated. The electronic band structures and the orbital projected density of states (PDOS) are presented in Fig. 7 and Fig. S4, Supplemental Material [53], respectively. Initially, electronic band structures are calculated at the level of GGA-PBE. Then, to analyze the band splitting near the energy band gap, the SOC effect is employed on top of PBE. The acquired results are summarized in Table II. Our calculations indicate that the inclusion of SOC slightly reduces the band gaps (except for GeS). The size of band-gap reduction (E_g^{PBE} - $E_g^{PBE-SOC}$) in γ-Ge_2SSe and γ-Ge_2SeTe monolayers is smaller than the γ-Ge_2STe nanosheet, which is due to the difference in size between the X and X' elements. HSE06 + SOC calculations yield similar band profiles but wider band gaps ($E_g^{HSE-SOC}$). It is found that all studied systems are semiconductors with indirect band gaps. $E_g^{HSE-SOC}$ is between 0.87 to 1.16 eV and spans a short range in the infrared part of the optical spectrum. It has been shown that materials with small band gaps are excellent candidates for applications in infrared-sensing devices [66,67]. In all

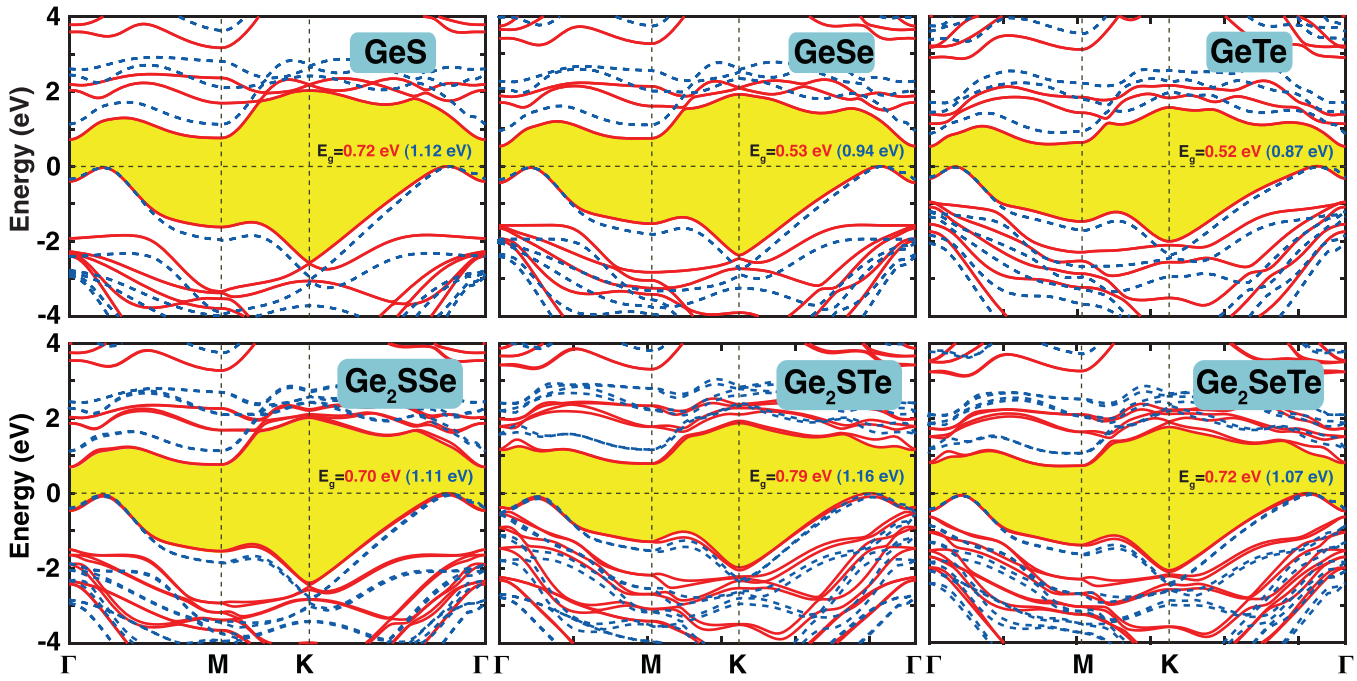

FIG. 7. The electronic band structures calculated at the level of GGA-PBE + SOC (red solid lines) and HSE06 + SOC (dashed blue lines), respectively. The fundamental band gaps are highlighted in yellow. The Fermi level is set to zero.

structures, the valence-band maxima (VBM) have a Mexican-hat dispersion that results in 1D van Hove singularity [26,68], offering remarkable electronic thermal transport properties. Moreover, the E-k curve of the bottom of the conduction-band minimum (CBM) has a parabolic dispersion with the minimum energy at Γ point in binary monolayers and Janus γ-Ge_2SSe, while in γ-Ge_2STe and γ-Ge_2SeTe crystals, the minimum energy is at the M point. We further analyzed the results of orbital PDOS to understand the characteristics of band edges. It is found that the VBM is mainly contributed from the Ge-s and X-p orbitals, while the electronic states near the CBM mainly belong to the p orbitals of Ge and X atoms. In ternary systems, VBM is mainly composed of Ge-s, X'-p, and X-p orbitals, whereas the CBM states are dominated by the p orbitals of Ge atoms.

F. Piezoelectric properties

The piezoelectric effect is the ability of generating an electric dipole moment as a response to the applied external stress (or vice versa) in noncentrosymmetric crystals. Piezoelectricity is a result of the electromechanical interaction, which is typically characterized by piezoelectric coefficients, i.e., piezoelectric stress tensors and piezoelectric strain tensors. Previous experimental observations and theoretical studies have demonstrated the improvement of piezoelectric constants in 2D materials compared to their three-dimensional (3D) counterparts [69]. The piezoelectric stress tensor, e_{ijk}, can be described as the coupling between electrical polarization (P_i) and strain tensor (ε_{jk}). e_{ijk} is formulated as follows:

$$e_{ijk} = \frac{\partial P_i}{\partial \varepsilon_{jk}}, \tag{2}$$

where i, j, and k indices correspond to the x, y, and z directions, respectively. In the 2D limit, e_{ij} must be renormalized by the length of the unit cell along the z axis, i.e., $e_{ij}^{2D} = z \times e_{ij}^{3D}$. The e_{ij}^{2D} can be obtained by the summation of electronic e_{ij}^{el} and ionic e_{ij}^{ion} contributions:

$$e_{ij} = e_{ij}^{el} + e_{ij}^{\text{ion}}. \tag{3}$$

The values of e_{ij} are determined using the DFPT method, and the piezoelectric strain tensors d_{ij} are related to e_{ij} and elastic constants C_{ij} via the following formula:

$$e_{ij} = d_{ik} C_{kj}. \tag{4}$$

The number of nonzero and unique piezoelectric tensors (e_{ij} and d_{ij}) is restricted by the symmetry of structures. For γ-GeX monolayers with D_{3d} symmetry, due to the inversion symmetry (the structures possess centrosymmetry), the piezoelectric constants are expected to be very small and can be neglected. For the Janus nanosheets with C_{3v} point-group symmetry, the nonzero elements of piezoelectric coefficients are e_{11} and d_{11}, as well as e_{31} and d_{31} for in-plane and out-of-plane piezoelectricity, respectively. The Voigt notation of the examined monolayers can be defined as

$$e = \begin{pmatrix} e_{11} & -e_{11} & 0 \\ 0 & 0 & -e_{11} \\ e_{31} & e_{31} & 0 \end{pmatrix}, \quad d = \begin{pmatrix} d_{11} & -d_{11} & 0 \\ 0 & 0 & -2d_{11} \\ d_{31} & d_{31} & 0 \end{pmatrix}.$$

The relations between these quantities and elastic constants are given by [35,69,70]

$$d_{11} = \frac{e_{11}}{c_{11} - c_{12}}, \quad d_{31} = \frac{e_{31}}{c_{11} + c_{12}}. \tag{5}$$

The calculated piezoelectric coefficients are listed in Table II. As can be seen, in the case of γ-GeX monolayers,

the values of e_{11} are found to be 0.6, 0.58, and 0.44 pC/m for γ-GeS, γ-GeSe, and γ-GeTe, respectively, which are noticeably small as compared to α-GeS monolayer (460 pC/m) [71]. The corresponding piezoelectric strain constants, d_{11}, are also negligibly small compared to the α-GeS monolayer. In addition, the out-of-plane piezoelectric tensors (e_{31} and d_{31}) are calculated, and the obtained results are found to be comparable to those of e_{11} and d_{11}. By going from binary to ternary, due to the broken in-plane and out-of-plane symmetries, the piezoelectric coefficients are considerably enhanced. The e_{11} coefficients of Janus are calculated to be 320, 683, and 396 pC/m for γ-Ge_2SSe, γ-Ge_2STe, and γ-Ge_2SeTe, respectively, and the corresponding d_{11} tensors are 5.76, 13.25, and 7.25 pm/V. The obtained values of d_{11} are larger than those reported for $XMoY$ and XWY Janus crystals [35]. For 2D ultrathin materials, large out-of-plane piezoelectricity is desirable for a variety of applications in electromechanical devices. The d_{31} coefficients are estimated to be 0.15, 0.32, and 0.19 pm/V for γ-Ge_2SSe, γ-Ge_2STe, and γ-Ge_2SeTe, respectively, which follow a trend similar to the reported values for Janus XGa_2X' monolayers [72]. These Janus monolayers with large piezoelectric responses represent a new class of 2D materials for a wide range of nanoscale piezoelectric applications, such as ultrasensitive mechanical detectors. In addition, we provided Table S2 in the Supplemental Material [53] to highlight and improve comparisons between the results of this study and other well-known 2D systems.

IV. CONCLUSION

In this paper, structural, vibrational, mechanical, electronic, and piezoelectric properties of single layers of γ-GeX and Janus γ-Ge_2XX' were investigated via *ab initio* calculations. The phonon-band dispersion, *ab initio* molecular dynamics simulations, and elastic tensor analysis verified the suggested monolayers' structural, dynamical, and mechanical stability. The heat capacity (C_V) of binary γ-GeX and ternary γ-Ge_2XX' systems is mainly contributed by in-plane LA-TA acoustic modes at a low-temperature regime, and as the temperature rises, it approaches the classical limit. Raman spectrum analysis showed that γ-GeX monolayers possess four Raman peaks, whereas Janus γ-Ge_2XX' structures exhibit additional six Raman-active modes stemming from the broken inversion symmetry. The mechanical response of the structures was found to be isotropic, and the computed results of in-plane stiffness (Y_{2D}) range from 66.46 to 73.25 N/m, indicating that the considered nanosheets are flexible. The estimated values of Poisson's ratio (ν) of Janus γ-Ge_2XX' monolayers lies between binary γ-GeX and γ-GeX' structures. It is also found that all examined systems are indirect-gap semiconductors with the Mexican hat dispersion in the valence band. The calculated band gaps at the level of HSE06+SOC are between 0.87 and 1.16 eV, which covers a part of infrared range of the optical spectrum. In addition, the piezoelectric coefficients were computed, and in-plane and out-of-plane piezoelectricity enhancement has been observed in Janus crystals. Our study reveals that binary γ-GeX and ternary γ-Ge_2XX' monolayers are stable materials with intriguing mechanical and electronic properties that make them suitable materials for diverse applications.

ACKNOWLEDGMENTS

B.S. acknowledges financial support from the Swedish Research Council (Grant No. 2022-04309). The computations were enabled in Project SNIC 2022/3-30 by resources provided by the Swedish National Infrastructure for Computing (SNIC) at NSC, PDC, and HPC2N, partially funded by the Swedish Research Council (Grant No. 2018-05973). B.S. acknowledges allocation of supercomputing hours by the PRACE DECI-17 project "Q2Dtopomat" at the Eagle Supercomputer in Poland and EuroHPC resources at the Karolina Supercomputer in the Czech Republic. B.S. and S.E. acknowledge EuroHPC resources at Finland's LUMI Supercomputer (through Projects No. EHPC-DEV-2022D10-059 and No. EHPC-DEV-2022D10-057).

[1] K. S. Novoselov, A. K. Geim, S. V. Morozov, D. Jiang, Y. Zhang, S. V. Dubonos, I. V. Grigorieva, and A. A. Firsov, Electric field effect in atomically thin carbon films, Science **306**, 666 (2004).

[2] R. Mas-Balleste, C. Gomez-Navarro, J. Gomez-Herrero, and F. Zamora, 2D materials: To graphene and beyond, Nanoscale **3**, 20 (2011).

[3] Q. H. Wang, K. Kalantar-Zadeh, A. Kis, J. N. Coleman, and M. S. Strano, Electronics and optoelectronics of two-dimensional transition metal dichalcogenides, Nat. Nanotechnol. **7**, 699 (2012).

[4] M. Chhowalla, H. S. Shin, G. Eda, L.-J. Li, K. P. Loh, and H. Zhang, The chemistry of two-dimensional layered transition metal dichalcogenide nanosheets, Nat. Chem **5**, 263 (2013).

[5] T. Das and J.-H. Ahn, Development of electronic devices based on two-dimensional materials, FlatChem **3**, 43 (2017).

[6] H. Liu, A. T. Neal, Z. Zhu, Z. Luo, X. Xu, D. Tománek, and P. D. Ye, Phosphorene: An unexplored 2D semiconductor with a high hole mobility, ACS Nano **8**, 4033 (2014).

[7] J. Qiao, X. Kong, Z.-X. Hu, F. Yang, and W. Ji, High-mobility transport anisotropy and linear dichroism in few-layer black phosphorus, Nat. Commun. **5**, 4475 (2014).

[8] W. Lu, H. Nan, J. Hong, Y. Chen, C. Zhu, Z. Liang, X. Ma, Z. Ni, C. Jin, and Z. Zhang, Plasma-assisted fabrication of monolayer phosphorene and its Raman characterization, Nano Res. **7**, 853 (2014).

[9] P. Yasaei, B. Kumar, T. Foroozan, C. Wang, M. Asadi, D. Tuschel, J. E. Indacochea, R. F. Klie, and A. Salehi-Khojin, High-quality black phosphorus atomic layers by liquid-phase exfoliation, Adv. Mater. **27**, 1887 (2015).

[10] J. Li, X. Zhang, Z. Chen, S. Lin, W. Li, J. Shen, I. T. Witting, A. Faghaninia, Y. Chen, A. Jain *et al.*, Low-symmetry rhombohedral GeTe thermoelectrics, Joule **2**, 976 (2018).

[11] S. Hao, F. Shi, V. P. Dravid, M. G. Kanatzidis, and C. Wolverton, Computational prediction of high thermoelectric performance in hole doped layered GeSe, Chem. Mater. **28**, 3218 (2016).

[12] B. Ul Haq, S. AlFaify, and A. Laref, Exploring novel flat-band polymorphs of single-layered germanium sulfide for high-efficiency thermoelectric applications, J. Phys. Chem. C **123**, 18124 (2019).

[13] D. D. Vaughn, R. J. Patel, M. A. Hickner, and R. E. Schaak, Single-crystal colloidal nanosheets of GeS and GeSe, J. Am. Chem. Soc. **132**, 15170 (2010).

[14] C. Li, L. Huang, G. P. Snigdha, Y. Yu, and L. Cao, Role of boundary layer diffusion in vapor deposition growth of chalcogenide nanosheets: The case of GeS, ACS Nano **6**, 8868 (2012).

[15] Y. Xu, H. Zhang, H. Shao, G. Ni, J. Li, H. Lu, R. Zhang, B. Peng, Y. Zhu, H. Zhu *et al.*, First-principles study on the electronic, optical, and transport properties of monolayer α-and β-GeSe, Phys. Rev. B **96**, 245421 (2017).

[16] Z. Hu, Y. Ding, X. Hu, W. Zhou, X. Yu, and S. Zhang, Recent progress in 2D group IV–IV monochalcogenides: Synthesis, properties and applications, Nanotechnology **30**, 252001 (2019).

[17] Y. Ye, Q. Guo, X. Liu, C. Liu, J. Wang, Y. Liu, and J. Qiu, Two-dimensional GeSe as an isostructural and isoelectronic analogue of phosphorene: Sonication-assisted synthesis, chemical stability, and optical properties, Chem. Mater. **29**, 8361 (2017).

[18] E. Sutter, B. Zhang, M. Sun, and P. Sutter, Few-layer to multilayer germanium (II) sulfide: Synthesis, structure, stability, and optoelectronics, ACS Nano **13**, 9352 (2019).

[19] F. Li, X. Liu, Y. Wang, and Y. Li, Germanium monosulfide monolayer: A novel two-dimensional semiconductor with a high carrier mobility, J. Mater. Chem. C **4**, 2155 (2016).

[20] G. Shi and E. Kioupakis, Anisotropic spin transport and strong visible-light absorbance in few-layer SnSe and GeSe, Nano Lett. **15**, 6926 (2015).

[21] G. Qin, Z. Qin, W.-Z. Fang, L.-C. Zhang, S.-Y. Yue, Q.-B. Yan, M. Hu, and G. Su, Diverse anisotropy of phonon transport in two-dimensional group IV–VI compounds: A comparative study, Nanoscale **8**, 11306 (2016).

[22] D. Zhang, S. Hu, Y. Sun, X. Liu, H. Wang, H. Wang, Y. Chen, and Y. Ni, XTe (X = Ge, Sn, Pb) monolayers: Promising thermoelectric materials with ultralow lattice thermal conductivity and high-power factor, ES Energy & Environment **10**, 59 (2020).

[23] J.-U. Lee, K. Kim, S. Han, G. H. Ryu, Z. Lee, and H. Cheong, Raman signatures of polytypism in molybdenum disulfide, ACS Nano **10**, 1948 (2016).

[24] X. Zhao, S. Ning, W. Fu, S. J. Pennycook, and K. P. Loh, Differentiating polymorphs in molybdenum disulfide via electron microscopy, Adv. Mater. **30**, 1802397 (2018).

[25] S. Y. Lim, J.-U. Lee, J. H. Kim, L. Liang, X. Kong, T. T. H. Nguyen, Z. Lee, S. Cho, and H. Cheong, Polytypism in few-layer gallium selenide, Nanoscale **12**, 8563 (2020).

[26] N. Luo, W. Duan, B. I. Yakobson, and X. Zou, Excitons and electron–hole liquid state in 2Dγ-phase group-IV monochalcogenides, Adv. Funct. Mater. **30**, 2000533 (2020).

[27] S. Lee, J.-E. Jung, H.-g. Kim, Y. Lee, J. M. Park, J. Jang, S. Yoon, A. Ghosh, M. Kim, J. Kim *et al.*, γ-GeSe: A new hexagonal polymorph from group IV–VI monochalcogenides, Nano Lett. **21**, 4305 (2021).

[28] X. Huang, R. Xiong, K. Volckaert, C. Hao, D. Biswas, M. Bianchi, P. Hofmann, P. Beck, J. Warmuth, B. Sa *et al.*, Experimental realization of semiconducting monolayer Si_2Te_2 films, Adv. Funct. Mater. **32**, 2208281 (2022).

[29] V. Van Thanh, N. D. Van, D. Van Truong, and N. T. Hung, Effects of strain and electric field on electronic and optical properties of monolayer γ-GeX (X = S, Se and Te), Appl. Surf. Sci. **582**, 152321 (2022).

[30] A.-Y. Lu, H. Zhu, J. Xiao, C.-P. Chuu, Y. Han, M.-H. Chiu, C.-C. Cheng, C.-W. Yang, K.-H. Wei, Y. Yang *et al.*, Janus monolayers of transition metal dichalcogenides, Nat. Nanotechnol. **12**, 744 (2017).

[31] J. Zhang, S. Jia, I. Kholmanov, L. Dong, D. Er, W. Chen, H. Guo, Z. Jin, V. B. Shenoy, L. Shi *et al.*, Janus monolayer transition-metal dichalcogenides, ACS Nano **11**, 8192 (2017).

[32] R. Li, Y. Cheng, and W. Huang, Recent progress of Janus 2D transition metal chalcogenides: From theory to experiments, Small **14**, 1802091 (2018).

[33] M. Demirtas, M. J. Varjovi, M. M. Cicek, and E. Durgun, Tuning structural and electronic properties of two-dimensional aluminum monochalcogenides: Prediction of JanusAl_2XX'(X/X': O, S, Se, Te) monolayers, Phys. Rev. Mater. **4**, 114003 (2020).

[34] M. Yagmurcukardes, F. M. Peeters, and H. Sahin, Electronic and vibrational properties of PbI_2: From bulk to monolayer, Phys. Rev. B **98**, 085431 (2018).

[35] L. Dong, J. Lou, and V. B. Shenoy, Large in-plane and vertical piezoelectricity in Janus transition metal dichalchogenides, ACS Nano **11**, 8242 (2017).

[36] T. Hu, F. Jia, G. Zhao, J. Wu, A. Stroppa, and W. Ren, Intrinsic and anisotropic Rashba spin splitting in Janus transition-metal dichalcogenide monolayers, Phys. Rev. B **97**, 235404 (2018).

[37] M. J. Varjovi, M. Yagmurcukardes, F. M. Peeters, and E. Durgun, Janus two-dimensional transition metal dichalcogenide oxides: First-principles investigation of WXO monolayers with X= S, Se, and Te, Phys. Rev. B **103**, 195438 (2021).

[38] M. Yagmurcukardes and F. M. Peeters, Stable single layer of Janus MoSO: Strong out-of-plane piezoelectricity, Phys. Rev. B **101**, 155205 (2020).

[39] W. Kohn and L. J. Sham, Self-consistent equations including exchange and correlation effects, Phys. Rev. **140**, A1133 (1965).

[40] P. Hohenberg and W. Kohn, Inhomogeneous electron gas, Phys. Rev. **136**, B864 (1964).

[41] G. Kresse and J. Hafner, *Ab initio* molecular dynamics for liquid metals, Phys. Rev. B **47**, 558 (1993).

[42] G. Kresse and J. Hafner, *Ab initio* molecular-dynamics simulation of the liquid-metal–amorphous-semiconductor transition in germanium, Phys. Rev. B **49**, 14251 (1994).

[43] G. Kresse and J. Furthmüller, Efficiency of *ab-initio* total energy calculations for metals and semiconductors using a plane-wave basis set, Comput. Mater. Sci. **6**, 15 (1996).

[44] G. Kresse and J. Furthmüller, Efficient iterative schemes for *ab initio* total-energy calculations using a plane-wave basis set, Phys. Rev. B **54**, 11169 (1996).

[45] P. E. Blöchl, Projector augmented-wave method, Phys. Rev. B **50**, 17953 (1994).

[46] J. P. Perdew, K. Burke, and M. Ernzerhof, Generalized Gradient Approximation Made Simple, Phys. Rev. Lett. **77**, 3865 (1996).

[47] M. Gmitra, S. Konschuh, C. Ertler, C. Ambrosch-Draxl, and J. Fabian, Band-structure topologies of graphene: Spin-orbit coupling effects from first principles, Phys. Rev. B **80**, 235431 (2009).

[48] J. Heyd, G. E. Scuseria, and M. Ernzerhof, Hybrid functionals based on a screened Coulomb potential, J. Chem. Phys. **118**, 8207 (2003).

[49] A. V. Krukau, O. A. Vydrov, A. F. Izmaylov, and G. E. Scuseria, Influence of the exchange screening parameter on the performance of screened hybrid functionals, J. Chem. Phys. **125**, 224106 (2006).

[50] H. J. Monkhorst and J. D. Pack, Special points for Brillouin-zone integrations, Phys. Rev. B **13**, 5188 (1976).

[51] A. Togo and I. Tanaka, First principles phonon calculations in materials science, Scr. Mater. **108**, 1 (2015).

[52] G. Henkelman, A. Arnaldsson, and H. Jónsson, A fast and robust algorithm for Bader decomposition of charge density, Comput. Mater. Sci. **36**, 354 (2006).

[53] See Supplemental Material at http://link.aps.org/supplemental/10.1103/PhysRevB.107.195421 for additional details on cohesive energies of α, β-GeX, and α-Ge_2SSe monolayers, planar average of the electrostatic potential diagrams, phonon density of states (PhDOS), *ab initio* molecular dynamics results at 600 K, and orbital projected density of states (PDOS) results of binary γ-GeX and ternary γ-Ge_2XX' (X/X' : S, Se, and Te) monolayers.

[54] Q. Wang, Q. Tan, Y. Liu, C. Qing, X. Feng, and D. Yu, Tunable electronic properties and giant spontaneous polarization in graphene/monolayer GeS van der Waals heterostructure, Phys. Status Solidi B **256**, 1900194 (2019).

[55] K. Ren, X. Ma, X. Liu, Y. Xu, W. Huo, W. Li, and G. Zhang, Prediction of 2D IV–VI semiconductors: Auxetic materials with direct-gap and strong optical absorption, Nanoscale **14**, 8463 (2022).

[56] F. Liu, P. Ming, and J. Li, *Ab initio* calculation of ideal strength and phonon instability of graphene under tension, Phys. Rev. B **76**, 064120 (2007).

[57] G. Qin, Z. Qin, H. Wang, and M. Hu, Anomalously temperature-dependent thermal conductivity of monolayer GaN with large deviations from the traditional 1/T law, Phys. Rev. B **95**, 195416 (2017).

[58] A. A. Balandin, Thermal properties of graphene and nanostructured carbon materials, Nat. Mater. **10**, 569 (2011).

[59] H. Sahin, Structural and phononic characteristics of nitrogenated holey graphene, Phys. Rev. B **92**, 085421 (2015).

[60] O. H. Nielsen and R. M. Martin, First-Principles Calculation of Stress, Phys. Rev. Lett. **50**, 697 (1983).

[61] Y. Le Page and P. Saxe, Symmetry-general least-squares extraction of elastic data for strained materials from *ab initio* calculations of stress, Phys. Rev. B **65**, 104104 (2002).

[62] M. Born and K. Huang, *Dynamical Theory of Crystal Lattices* (Clarendon Press, Oxford, 1954)

[63] F. Mouhat and F.-X. Coudert, Necessary and sufficient elastic stability conditions in various crystal systems, Phys. Rev. B **90**, 224104 (2014).

[64] W. Shi and Z. Wang, Mechanical and electronic properties of Janus monolayer transition metal dichalcogenides, J. Phys.: Condens. Matter **30**, 215301 (2018).

[65] R. M. Christensen, Mechanisms and measures for the ductility of materials failure, Proc. R. Soc. A. **476**, 20190719 (2020).

[66] M. Long, A. Gao, P. Wang, H. Xia, C. Ott, C. Pan, Y. Fu, E. Liu, X. Chen, W. Lu *et al.*, Room temperature high-detectivity mid-infrared photodetectors based on black arsenic phosphorus, Sci. Adv. **3**, e1700589 (2017).

[67] W. C. Tan, L. Huang, R. J. Ng, L. Wang, D. M. N. Hasan, T. J. Duffin, K. S. Kumar, C. A. Nijhuis, C. Lee, and K.-W. Ang, A black phosphorus carbide infrared phototransistor, Adv. Mater. **30**, 1705039 (2018).

[68] T. Cao, Z. Li, and S. G. Louie, Tunable Magnetism and Half-Metallicity in Hole-Doped Monolayer GaSe, Phys. Rev. Lett. **114**, 236602 (2015).

[69] M. N. Blonsky, H. L. Zhuang, A. K. Singh, and R. G. Hennig, *Ab initio* prediction of piezoelectricity in two-dimensional materials, ACS Nano **9**, 9885 (2015).

[70] M. Yagmurcukardes, C. Sevik, and F. M. Peeters, Electronic, vibrational, elastic, and piezoelectric properties of monolayer Janus MoSTe phases: A first-principles study, Phys. Rev. B **100**, 045415 (2019).

[71] R. Fei, W. Li, J. Li, and L. Yang, Giant piezoelectricity of monolayer group IV monochalcogenides: SnSe, SnS, GeSe, and GeS, Appl. Phys. Lett. **107**, 173104 (2015).

[72] Y. Guo, S. Zhou, Y. Bai, and J. Zhao, Enhanced piezoelectric effect in Janus group-III chalcogenide monolayers, Appl. Phys. Lett. **110**, 163102 (2017).